NANO · MICRO small
www.small-journal.com

Hybrid Nanomedicine Fabricated from Photosensitizer-Terminated Metal–Organic Framework Nanoparticles for Photodynamic Therapy and Hypoxia-Activated Cascade Chemotherapy

Zhimei He, Yunlu Dai, Xiangli Li, Dan Guo, Yijing Liu, Xiaolin Huang, Jingjing Jiang, Sheng Wang, Guizhi Zhu, Fuwu Zhang, Lisen Lin, Jun-Jie Zhu, Guocan Yu,* and Xiaoyuan Chen**

During photodynamic therapy (PDT), severe hypoxia often occurs as an undesirable limitation of PDT owing to the O_2-consuming photodynamic process, compromising the effectiveness of PDT. To overcome this problem, several strategies aiming to improve tumor oxygenation are developed. Unlike these traditional approaches, an opposite method combining hypoxia-activated prodrug and PDT may provide a promising strategy for cancer synergistic therapy. In light of this, azido-/photosensitizer-terminated UiO-66 nanoscale metal–organic frameworks (UiO-66-H/N_3 NMOFs) which serve as nanocarriers for the bioreductive prodrug banoxantrone (AQ4N) are engineered. Owing to the effective shielding of the nanoparticles, the stability of AQ4N is well preserved, highlighting the vital function of the nanocarriers. By virtue of strain-promoted azide–alkyne cycloaddition, the nanocarriers are further decorated with a dense PEG layer to enhance their dispersion in the physiological environment and improve their therapeutic performance. Both in vitro and in vivo studies reveal that the O_2-depleting PDT process indeed aggravates intracellular/tumor hypoxia that activates the cytotoxicity of AQ4N through a cascade process, consequently achieving PDT-induced and hypoxia-activated synergistic therapy. Benefiting from the localized therapeutic effect of PDT and hypoxia-activated cytotoxicity of AQ4N, this hybrid nanomedicine exhibits enhanced therapeutic efficacy with negligible systemic toxicity, making it a promising candidate for cancer therapy.

1. Introduction

Photodynamic therapy (PDT) is an emerging treatment modality that can be turned on by remote laser illumination at the region of interest.[1–4] Three vital components, namely, photosensitizer, O_2, and specific exciting light are included in PDT.[5–8] Upon exposure to specific laser irradiation, photosensitizer can be promoted to an excited triplet state, and transfer energy to surrounding O_2 to generate reactive oxygen species (ROS), especially singlet oxygen ($^1O_2$) that strikes the intracellular redox balance and consequently activates ROS-mediated apoptosis.[9–11] Such O_2-dependent photodynamic process always consumes massive O_2 to exacerbate tumor hypoxia that will in turn discount the PDT efficacy,[12–15] as well as promote tumor resistance to therapies (e.g., radiotherapy),[16] accounting for the tumor recurrence. Unlike the common strategies of elevating O_2 amount to relieve tumor hypoxia,[6,16–20] an opposite method by fully taking advantage of the severe hypoxia caused by PDT to activate chemotherapy may provide a promising strategy

Dr. Z. He, X. Li, D. Guo, Prof. J.-J. Zhu
State Key Laboratory of Analytical Chemistry for Life Science
School of Chemistry and Chemical Engineering
Nanjing University
Nanjing 210023, P. R. China
E-mail: jjzhu@nju.edu.cn
Dr. Y. Dai
Faculty of Health Sciences
University of Macau
Macau SAR 999078, P. R. China
The ORCID identification number(s) for the author(s) of this article can be found under https://doi.org/10.1002/smll.201804131.
Dr. Y. Dai, Dr. Y. Liu, Dr. X. Huang, Dr. S. Wang, Dr. G. Zhu, Dr. F. Zhang, Dr. L. Lin, Dr. G. Yu, Prof. X. Chen
Laboratory of Molecular Imaging and Nanomedicine (LOMIN)
National Institute of Biomedical Imaging and Bioengineering (NIBIB)
National Institutes of Health (NIH)
Bethesda, MD 20892, USA
E-mail: guocanyu@zju.edu.cn; shawn.chen@nih.gov
Dr. J. Jiang
State Key Laboratory of Coordination Chemistry
School of Chemistry and Chemical Engineering
Nanjing University
Nanjing 210023, P. R. China

DOI: 10.1002/smll.201804131

for cancer therapy.[21–23] In this case, hypoxia-activated prodrugs (e.g., triapazamine,[24] apaziquone[25]) undergo metabolism to become toxic species in O_2-deficient environment. Banoxantrone (AQ4N) is one of such prodrugs that can be enzymatically reduced to toxic AQ4 by endogenous inducible nitric oxide synthase (iNOS) and cytochrome P450 (CYP) isozymes under hypoxia.[26,27] However, under normoxic condition, O_2 molecule outcompetes AQ4N for the active site of CYPs, thus efficiently inhibiting the enzymatic activation of AQ4N.[25] We hypothesize that a cascade strategy of PDT-induced O_2 depletion and subsequent bioreduction of hypoxia-activated prodrug is expected to synergistically eradicate cancer cells and enhance therapeutic efficacy. To realize this, smart nanomaterials capable of codelivering prodrug and photosensitizer are urgently required. Given that most of the hypoxia-activated prodrugs (e.g., triapazamine, AQ4N) are hydrophilic, most polymeric nanoparticles (PNPs) fabricated from amphiphilic copolymers may not meet this requirement owing to their poor loading efficiency of these hydrophilic molecules. Therefore, it is necessary to develop other nanocarriers which favor efficient prodrug loading and programmable prodrug release.

Nanoscale metal–organic frameworks (NMOFs) emerged as hybrid porous nanomaterials are built from metal ions/clusters and bridging ligand via coordination interactions.[28,29] Benefiting from their high porosity, large surface area, and tailorable surface chemistry, NMOFs represent appealing nanocarriers for cargo payloads, providing great promise for biomedical applications.[28] In the case of highly crystalline UiO-66 NMOFs, Zr_6 clusters as metal nodes together with terephthalic acid as bridging ligand constitute the highly porous structure.[30,31] Their microporous cages and excellent stability make them promising candidates for drug encapsulation.[32–35] Moreover, synthetic modulators can be incorporated during synthesis or postmodification of UiO-66, which endows the nanoparticles (NPs) with external surface modifiability or functionality.[36–39] In view of their high stability and tunable external surface engineering, the UiO-66 NPs are suitable nanovehicles for cargo delivery.

Herein, we report an intelligent nanosystem based on UiO-66 NPs for photodynamic therapy and hypoxia-triggered cascade chemotherapy. As depicted in **Scheme 1**, photosensitizer photochlor (HPPH) and azide group coanchored UiO-66 NPs (UiO-66-H/N_3) are incorporated via a one-pot solvothermal method. The external azide groups facilitate the further PEGylation through copper-free click reaction that endows the NPs with the enhanced stability and improved PDT performance. Meanwhile, the porosity of the NPs is well-suited for encapsulation of AQ4N to protect the bioreductive prodrug from degradation during circulation. In this system, AQ4N release is demonstrated to be phosphate ion-sensitive. Typically, negligible AQ4N release is found in low concentration of PBS (2.00×10^{-3} M) while fast and nearly complete AQ4N release occurs in high concentration of PBS ($\geq 10.0 \times 10^{-3}$ M). Considering the low concentration of phosphate in plasma/extracellular fluid ($\approx 2.00 \times 10^{-3}$ M) and the high concentration of phosphate within cells[40] especially in endosomes,[32] prodrug release can be mostly inhibited during delivery while be switched on after internalization due to the

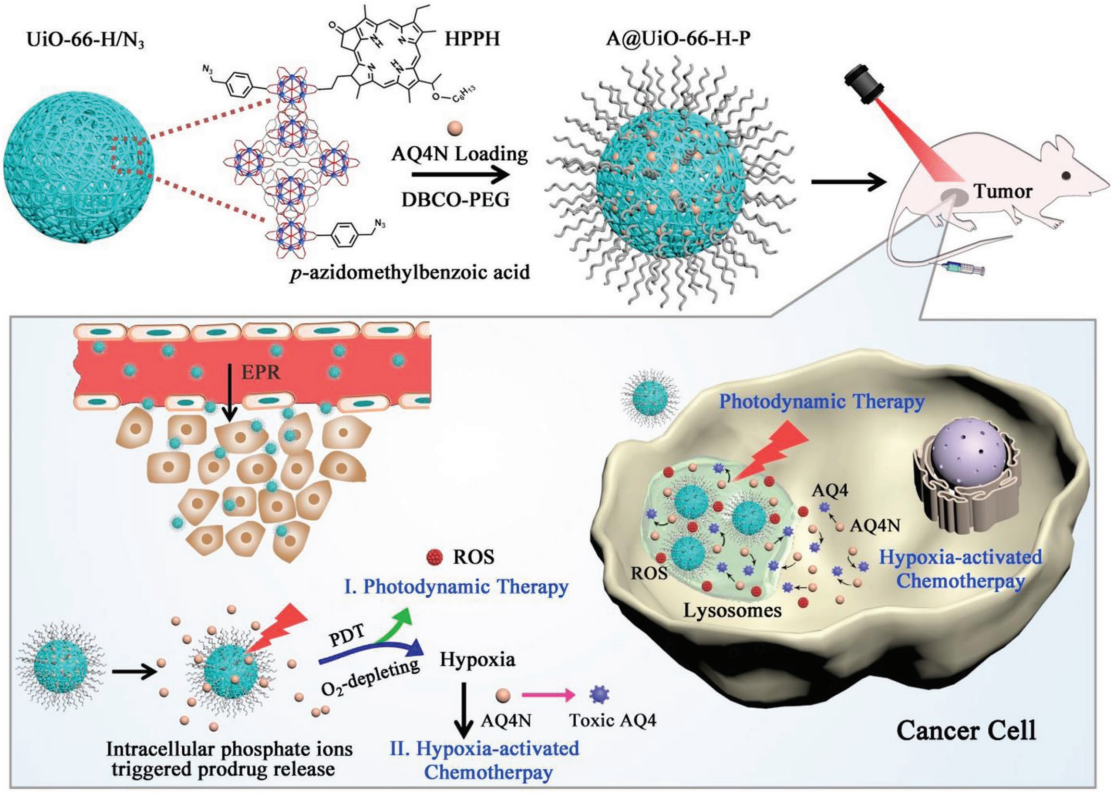

Scheme 1. Schematic illustration showing the synthetic procedure of A@UiO-66-H-P NPs and the mechanism of photodynamic therapy and hypoxia-activated cascade chemotherapy.

presence of much higher concentration of phosphate inside cells, which helps prevent premature leakage and achieve on-demand prodrug release. Both in vitro and in vivo results demonstrate that the toxicity of AQ4N is indeed enzymatically turned on by hypoxia arising from O_2-consuming photodynamic process, thus contributing to the enhanced tumor suppression.

2. Results and Discussion

2.1. Preparation of A@UiO-66-H-P NPs with Phosphate Ions-Sensitive AQ4N Release

In this study, UiO-66 NPs are selected as nanocarriers owing to their tunable external surface property and microporous cages. The size and morphology of UiO-66 NPs can be fine-tuned by introducing monocarboxyl molecules (e.g., benzoic acid,[33,37,38] *p*-azidomethylbenzoic acid[33]) during synthesis. Such modulators function as capping agents to decorate the external surface of NPs that may introduce functional groups for further modification. Thus, UiO-66-H/N_3 with HPPH/azide groups on the external surface were fabricated through a one-step solvothermal method in which monocarboxyl HPPH and *p*-azidomethylbenzoic acid (Figure S1, Supporting Information) were utilized as the functionalized modulators. As illustrated in **Figure 1**a and Figure S2 (Supporting Information), uniform UiO-66-H/N_3 NPs with a diameter around 75 nm were obtained. Compared with white UiO-66-N_3 without HPPH, the appearance of brownish green and the distinguishable adsorption of HPPH in UiO-66-H/N_3, collectively confirmed the successful incorporation of HPPH (Figure 1b). The incorporation contents of HPPH and p-azidomethylbenzoic in the UiO-66-H/N_3 NPs were calculated to be 0.38 and 1.34%, respectively, from the corresponding standard calibration curve (Figure S3, Supporting Information). Since the modulators facilitated the external surface functionalization and would not occupy the pores of NPs,[33,41] we adopted UiO-66-N_3 instead of UiO-66-H/N_3 to investigate the azidation and prodrug payload. As characterized by Fourier transform infrared (FTIR) spectroscopy, the obvious band at 2100 cm^{-1} of $\nu(N_3)$ proved the efficient modification of azide groups on the NMOFs (Figure S4, Supporting Information). The N_2 sorption isotherms results revealed that UiO-66-N_3 NPs possessed a high surface area (1453 $m^2\ g^{-1}$) and large pore volume (0.74 $cm^3\ g^{-1}$), implying their potential application for cargo loading (Figure S5 and Table S1, Supporting Information). Next, hypoxia-activated prodrug AQ4N was encapsulated into the NPs driven by the strong complexation between AQ4N and Zr^{4+} centers and π–π interactions between AQ4N and the organic ligands (e.g., terephthalic acid, benzoic acid). Compared with UiO-66-N_3, the AQ4N-loaded UiO-66-N_3 (A@UiO-66-N_3) showed decreased surface area along with reduced pore volume but exhibited less variation in pore size distribution (Figure S5 and Table S1, Supporting Information). These results were in accordance with previous report,[33] suggesting that AQ4N molecules were attaching to the particle surface instead of blocking the pores. As shown in Figure S6 (Supporting Information), adsorption of AQ4N was clearly observed in AQ4N-loaded UiO-66-H/N_3 NPs (A@UiO-66-H). By virtue of UV–vis measurements, the AQ4N loading capacity was calculated to be 69.0 mg g^{-1} via subtracting the supernatant from the total prodrug (Figure S7, Supporting Information). Such prodrug payload had little influence on the crystal structure of UiO-66-N_3 NPs as confirmed by powder X-ray diffraction (PXRD) (Figure S8, Supporting Information). Interestingly, the UV–vis absorption of AQ4N in A@UiO-66-H showed negligible decrease after being placed at room

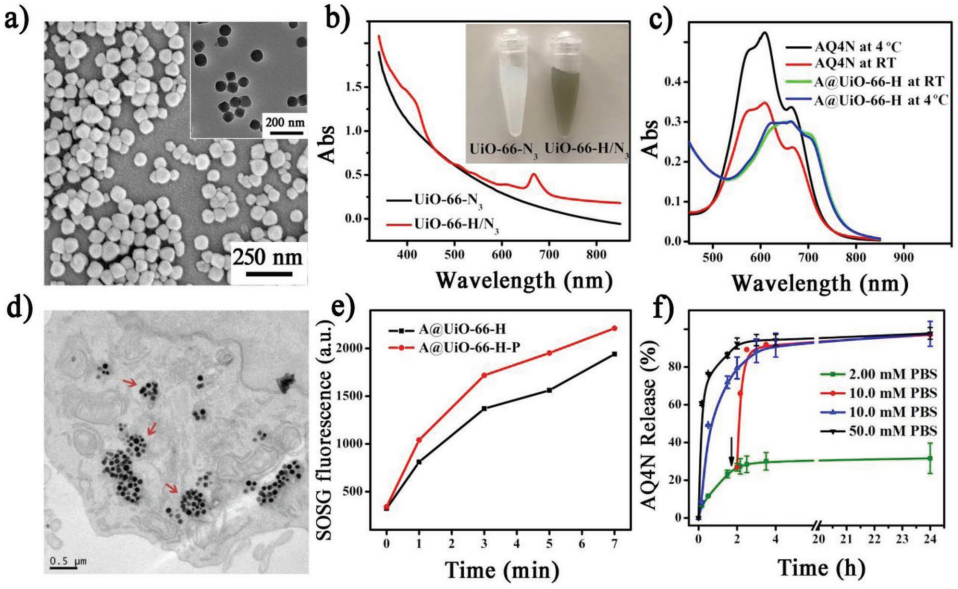

Figure 1. a) SEM image of UiO-66-H-N_3 NPs. Inset is the TEM image. b) UV–vis spectra of UiO-66-N_3 NPs and UiO-66-H/N_3 NPs. Inset are the corresponding photos. c) UV–vis spectra of AQ4N and A@UiO-66-H after being kept at 4 °C and RT for 48 h. d) The bio-TEM image of U87MG cells after 24 h incubation with A@UiO-66-H-P. The arrows point at the locations of lysosomes. e) The change of SOSG fluorescence intensity with increasing laser irradiation duration. f) AQ4N release from UiO-66-A-P NPs under different concentrations of PBS (2.00, 10.0, and 50.0 × 10^{-3} M). Particularly, in the case of red line, the concentration of PBS increased from 2.00 to 10.0 × 10^{-3} M at 2 h time point.

temperature (RT) for 48 h while significant decrease was found for free AQ4N (Figure 1c). This result implied that the encapsulation of AQ4N into UiO-66-H/N_3 was conducive to maintain the stability of AQ4N owing to the efficient shielding by the NPs. To stabilize the NPs in physiological environment, PEGylation was conducted through copper-free click chemistry between external azide groups on the NPs and DBCO-PEG (Figures S9 and S10, Supporting Information). The average hydrodynamic diameter of the resultant NPs (A@UiO-66-H-P NPs) was around 95 nm (Figure S11, Supporting Information). The assembly process was monitored via FTIR, dynamic light scattering (DLS), and zeta potential. Accompanied with the appearance of ν(C—H), the characteristic peak related to the azide groups apparently disappeared (Figure S4, Supporting Information), demonstrating that the exterior azide groups were consumed due to the PEGylation. Moreover, both the increase in hydrodynamic diameter and the decrease in zeta potential also confirmed the successful PEGylation (Figure S12, Supporting Information). Benefiting from the external surface modification with PEG, the dispersity of the NPs was greatly improved as no precipitate was observed after 24 h dispersion in saline solution while the NPs without PEGylation aggregated severely (Figure S13, Supporting Information). No significant variation in diameter was found during 24 h dispersion in both 2.00×10^{-3} M PBS in the absence or presence of 10% fetal bovine serum (FBS) (Figure S14, Supporting Information). Besides, as revealed by bio-transmission electron microscopy (TEM) images, intact NPs were identified in lysosomes after internalization into U87MG cells (Figure S15, Supporting Information and Figure 1d). All these results collectively confirmed the excellent stability of the NPs. Since phosphate ion has a high affinity for Zr(IV), it may promote the degradation of NMOFs.[32] In this regard, the release amount of *p*-azidomethylbenzoic acid from UiO-66-N_3 NPs, which is indicative of the stability of the NPs, was quantified by high-performance liquid chromatography (HPLC) analysis. As displayed in Figure S16 (Supporting Information), the release rate was very slow and only 24% of *p*-azidomethylbenzoic was liberated after 24 h exposure to 2.00×10^{-3} M PBS, confirming that the low concentration of PBS (2.00×10^{-3} M) was unable to destroy the highly crystalline UiO-66-N_3 NPs. Given that the concentration of phosphate in plasma/extracellular fluids is about 2.00×10^{-3} M,[40] the NPs would remain mostly intact during delivery to avoid premature drug release, possibly reducing side effects toward normal tissues. Then the ROS production capability of the nanomaterials was investigated by detecting the decay of anthracene-9,10-dipropionic acid disodium salt (ADPA) absorption at 408 nm.[42,43] Laser irradiation resulted in little absorption change, whereas significant adsorption decrease was observed in the group of UiO-66-H-P NPs without AQ4N under laser irradiation, which confirmed the efficient production of ROS. It should be noted that the further encapsulation of AQ4N did not affect their performance of ROS generation (Figure S17, Supporting Information). The PEGylation helps to improve the dispersity of the NPs in physiological saline, which is expected to elevate the generation rate of $^1O_2$ by overcoming the quenching effect caused by the aggregation of the photosensitizers. To verify this, a $^1O_2$ sensor green reagent SOSG that produces intense fluorescence in the presence of $^1O_2$ was adopted to evaluate the production of $^1O_2$.[44] Under laser irradiation, the A@UiO-66-H-P NPs appreciably outperformed A@UiO-66-H in generating $^1O_2$ (Figure 1e), which highlighted the importance of PEGylation to enhance the PDT performance. The A@UiO-66-H-P NPs exhibited phosphate ion-activated prodrug release behavior. As depicted in Figure 1f, the prodrug release was slow at low concentration of PBS (2.00×10^{-3} M). However, upon exposure to higher concentration of PBS (10.0 or 50.0×10^{-3} M), fast and almost complete AQ4N release was observed. This is attributed to the much stronger chelating ability of phosphate ions that outcompete AQ4N from Zr^{4+} center. Considering the rather high concentration of phosphate inside cells than that in extracellular fluids ($\approx 2.00 \times 10^{-3}$ M),[32,40] AQ4N would be promptly released once internalized into cancer cells, which prevents premature release and realizes on-demand prodrug release. The localized therapeutic effect of PDT along with the PDT-induced and hypoxia-activated toxicity of AQ4N will further minimize the undesirable side effects.

2.2. Cellular Uptake and ROS Production of A@UiO-66-H-P NPs

We then performed methyl thiazolyl tetrazolium (MTT) assay to test the cytotoxicity of the A@UiO-66-H-P NPs against U87MG cells. The NPs exhibited negligible cell growth inhibition rate even after 48 h incubation at a concentration of 100 μg mL^{-1} (Figure S18, Supporting Information), which demonstrated their good biocompatibility. Then confocal laser scanning microscopy (CLSM) and flow cytometric analysis were utilized to investigate the cellular uptake of the A@UiO-66-H-P NPs. As displayed in the CLSM images (Figure S19, Supporting Information), strong red fluorescence corresponding to HPPH on the NPs was observed in U87MG cells, which manifested the substantial cellular uptake of the NPs. Flow cytometric results further revealed that such cellular internalization increased over time (**Figure 2**a). The endocytic pathways of the NPs into U87MG cells were then explored using CLSM in the presence of different biochemical inhibitors. Typically, micropinocytosis, clathrin-mediated internalization, and caveolae-mediated pathway are blocked by amiloride, sucrose, and genistein, respectively.[45–48] We found that cellular uptake of the A@UiO-66-H-P NPs was appreciably suppressed at 4 °C, which implied that the endocytic process was energy-dependent. Obvious inhibition in internalization of the NPs was observed in both sucrose- and genistein-treated U87MG cells, whereas little influence was found in the case of amiloride-treated cells (Figure 2b). Quantitative assay using flow cytometry (Figure S20, Supporting Information) showed the same trend. These results suggested that the NPs were mainly taken up by U87MG cells through clathrin- and caveolae-mediated pathways rather than micropinocytosis, indicating that the NPs were prevailingly internalized into cells via endosome/lysosomal transportation. This was further verified by the colocalization analysis as the red fluorescence of the NPs overlapped well with the green fluorescence arising from LysoTracker Green (Figure S21, Supporting Information). Next, the intracellular $^1O_2$ production capacity of the A@UiO-66-H-P NPs was assessed using a commercially available ROS probe 2′,7′-dichlorofluorescin diacetate (DCFH-DA).[7] At physiological condition within cells, DCFH-DA is deacetylated into DCFH.

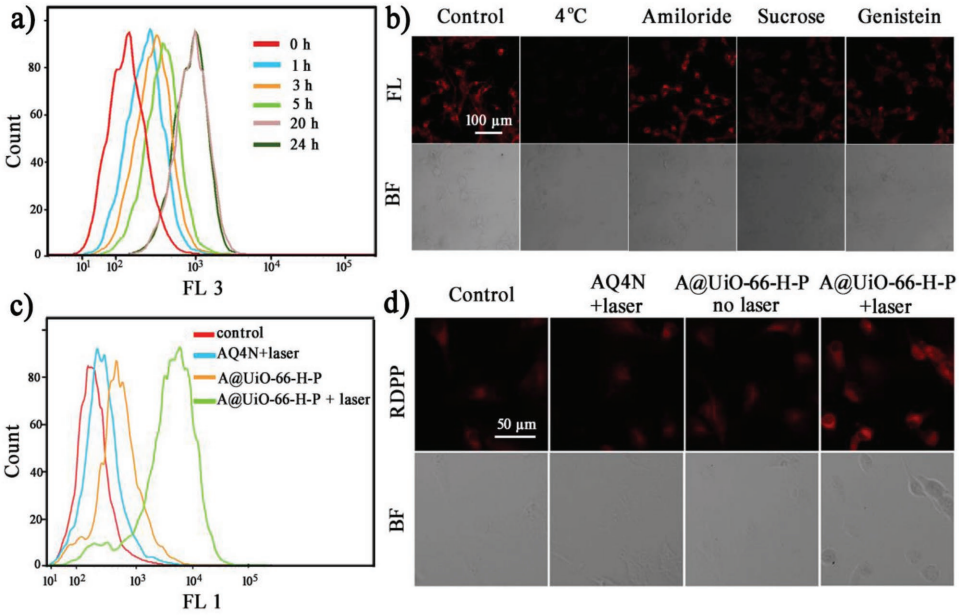

Figure 2. a) Flow cytometry analysis of U87MG cells after incubation with A@UiO-66-H-P NPs (20.0 μg mL^{-1}) for different periods of time (0, 1, 3, 5, 20, and 24 h). b) CLSM images reveal the mechanisms of cellular uptake by U87MG cells. c) Intracellular ROS level of U87MG cells after various treatments. d) CLSM images illustrating intracellular O_2 level by an O_2 probe $[Ru(dpp)_3]Cl_2$.

In the presence of ROS, DCFH is oxidized to form fluorescent DCF to reflect the intracellular ROS level.[49,50] Weak fluorescence was detected in both AQ4N and A@UiO-66-H-P treated U87MG cells in the absence of laser irradiation. In sharp contrast, after 671 nm laser irradiation (100 mW cm^{-2}, 6 min), the A@UiO-66-H-P treated cells emitted much intense green fluorescence (Figure S22, Supporting Information), suggesting a significant promotion in intracellular ROS level following the photodynamic process. A similar trend was observed in the flow cytometric result that further validated the good performance of the NPs as a PDT agent (Figure 2c). This PDT process converts O_2 to $^1O_2$, resulting in severe hypoxia. A commercial O_2 sensor ($[Ru(dpp)_3]Cl_2$) was employed to assess the intracellular O_2 level, whose fluorescence could be quenched by O_2.[51] U87MG cells cultured with free AQ4N combined with laser or A@UiO-66-H-P without irradiation were utilized as controls. Negligible fluorescence was detected in these control groups because of their normoxic environment. By contrast, A@UiO-66-H-P treated cells displayed much stronger fluorescence after laser irradiation (Figure 2d), indicating that the hypoxia indeed took place owing to the O_2-consuming PDT process.

2.3. In Vitro Combined Therapy and Penetration of A@UiO-66-H-P NPs

Under hypoxia, inactive AQ4N undergoes enzymatic reduction by endogenous iNOS and CYP isozymes,[25] and the reduced product (active AQ4) possesses strong DNA binding affinity and topoisomerase inhibition, which imposes a great damage to hypoxic cells.[25] To verify it, we carried out MTT experiments in which U87MG cells were treated with free AQ4N or A@UiO-66-H-P under normoxic (20%) or hypoxic (1%) condition. As given in **Figure 3**a, both AQ4N and A@UiO-66-H-P presented remarkably higher cell mortality rate under hypoxia than those under normoxia condition. This result revealed that A@UiO-66-H-P could selectively and efficiently kill hypoxic cells by virtue of the hypoxia-driven cytotoxicity of AQ4N. Based on this, we explored the combination anticancer effect between the photosensitizer (HPPH) and the therapeutic prodrug (AQ4N) using MTT assay. U87MG cells still remained high cell survival rate after treatment with UiO-66-H-P, A@UiO-66-H-P or free AQ4N (Figure 3b). In sharp contrast, apparent cell inhibition was observed for the cells administered with single PDT (UiO-66-H-P) and photo-chemotherapy (A@UiO-66-H-P). It is noted that UiO-66-H-P and A@UiO-66-H-P displayed parallel ROS generation capacity (Figure S17, Supporting Information), however, A@UiO-66-H-P presented much higher phototoxicity compared with UiO-66-H-P. The improved anticancer ability is apparently attributed to hypoxia-activated chemotherapy arising from O_2-depleting PDT process. To visually compare the therapeutic effect, live/dead cytotoxicity kit was used to distinguish cell viability, in which live cells were stained with calcium AM (green) and the dead cells were stained with propidium iodide (PI, red). As shown in Figure 3c, widespread green signal and little red signal were observed in the groups treated with laser or A@UiO-66-H-P only, which indicated high cell viability under these conditions. Comparatively, obvious red signal was clearly observed for the cells treated with UiO-66-H-P or A@UiO-66-H-P followed by laser irradiation. Particularly, A@UiO-66-H-P exhibited much stronger cytotoxicity after irradiation as less green signal was detected along with lower cell density. Taken together, A@UiO-66-H-P shows high potency in PDT-induced and hypoxia-triggered chemotherapy.

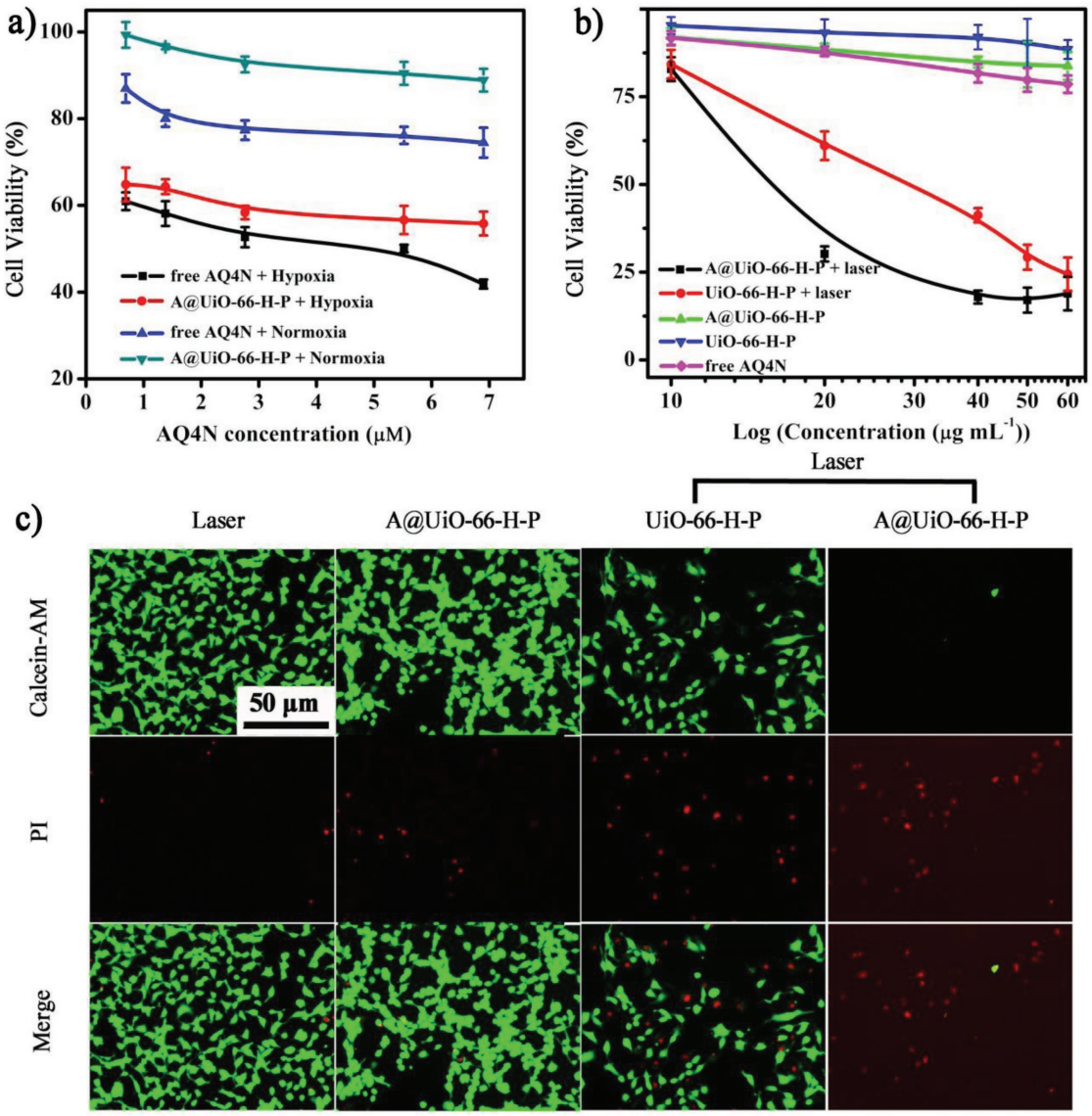

Figure 3. a) Effects of free AQ4N and A@UiO-66-H-P NPs on U87MG cells under hypoxia and normoxia conditions. b) Cell survival rate and c) live/dead assay of U87MG cells after various treatments.

2.4. Tumor Accumulation and Cascade Therapy of A@UiO-66-H-P NPs

For in vivo therapy, tumor penetration of NPs should be guaranteed. Since 3D multicellular tumor spheroid (3D MCTS) reasonably mimics tumor microenvironment,[52,53] U87MG cell-based MCTS was then adopted to investigate the penetration of the A@UiO-66-H-P. The established MCTS with a diameter around 400 μm was cultured with A@UiO-66-H-P (50.0 μg mL^{-1}) for 24 h and then subjected to CLSM observation. 34 Z-stack CLSM images were acquired via top to down scanning (Figure S23, Supporting Information). Three representative images were selected as top, middle, and bottom sections (**Figure 4**a), respectively. The Z-stack images were then reconstructed into 3D images using Image J (Figure 4b). From the above results, we found that the blue fluorescence from the nuclear marker (DAPI) only distributed on the rim of MCTS owing to the poor penetration of blue laser. Inversely, red signal of A@UiO-66-H-P spread throughout the MCTS, revealing the good penetration of the A@UiO-66-H-P NPs.

The enhanced permeability and retention (EPR) effect of tumor favors the accumulation of NPs in tumor site. Tumor accumulation of A@UiO-66-H-P NPs was then studied by recording the fluorescence of HPPH in the tumor region. Tumor slice was prepared at 24 h after intravenous (i.v.) injection and visualized by CLSM. As shown in **Figure 5**a, intense red fluorescence of HPPH decorated NPs was seen across the tumor slice. Fluorescence intensity variation along the marked yellow line further proved the existence of A@UiO-66-H-P NPs according to the high red fluorescence intensity (Figure 5b). These results demonstrated that the NPs could accumulate well in the tumor site. To further quantify the

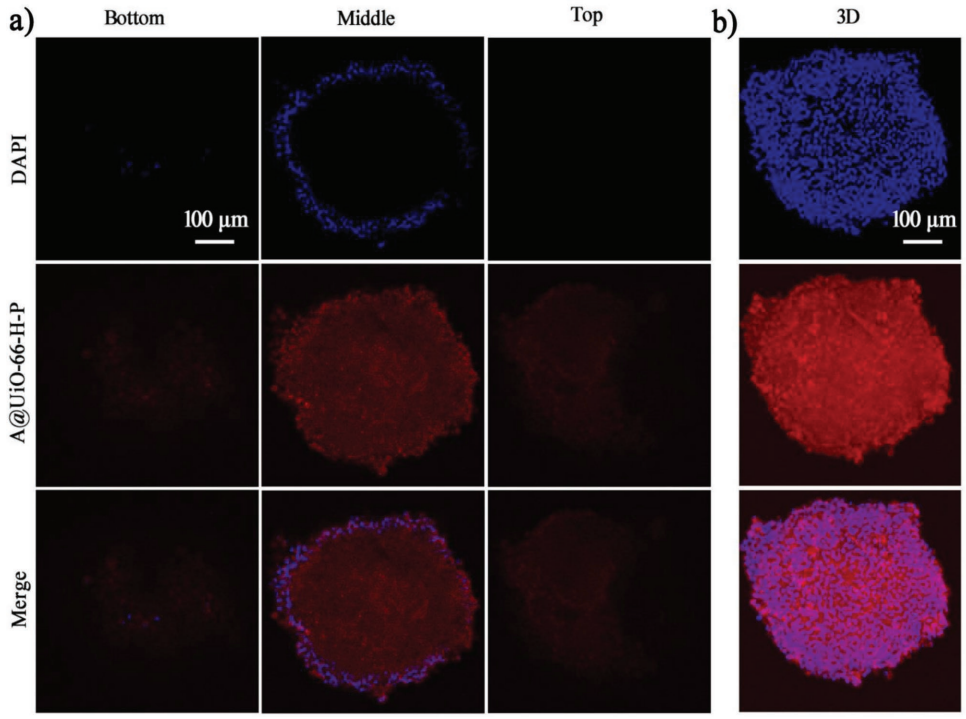

Figure 4. Penetration of A@UiO-66-H-P in U87MG spheroid. a) Three representative images from the top, middle, and bottom sections. b) 3D reconstruction of the Z-stack images. Blue fluorescence corresponds to DAPI-stained nucleus while the red fluorescence comes from A@UiO-66-H-P NPs.

accumulation amount, in vivo biodistribution of A@UiO-66-H-P was studied by determining the Zr content in the tissues using inductively coupled plasma optical emission spectrometry (ICP-OES). As seen in Figure S24 (Supporting Information), tumor accumulation was determined to be 3.5% at 24 h post i.v. injection.

Our design is based on the O_2-consuming PDT process which can generate hypoxia, and subsequently activate the toxicity of AQ4N. Hypoxia-inducible factor 1α (HIF1-α) immunofluorescence staining[15,54] was then performed to indirectly analyze the O_2 level in the tumor. For the mice treated with laser irradiation at 671 nm (100 mW cm^{-2}) for 10 min, no hyperthermia effect was generated, as evidenced by the negligible temperature increase at tumor sites captured by NIR camera (Figures S25 and S26, Supporting Information), which suggested the safety of the applied laser. Notably, obviously enhanced green fluorescence was observed in the tumor site from the mice injected with A@UiO-66-H-P followed by laser irradiation at 24 h time point (Figure 5c). This consequence indicated significant decreased O_2 level after laser exposure, thus confirming that in vivo PDT process indeed aggravated the tumor hypoxia. Such PDT-induced hypoxia is anticipated to favor the activation of chemotherapy to achieve synergistic therapy. To prove it, anticancer effect of HPPH/AQ4N mixture, UiO-66-H-P, and A@UiO-66-H-P was investigated on U87MG tumor-bearing (Figure 5d). Compared with the saline-treated control group, the mice treated with HPPH/AQ4N mixture only exhibited limited tumor suppression after laser exposure. This was likely attributed to the poor tumor accumulation along with the fast excretion of both HPPH and AQ4N. For the mice treated with A@UiO-66-H-P alone or UiO-66-H-P plus laser irradiation, moderate tumor inhibition rate was observed. By contrast, A@UiO-66-H-P NPs followed by laser irradiation outperformed any single modality treatment in antitumor performance, survival rate, and survival time (Figure 5d–f), strongly confirming the synergistic PDT and hypoxia-activated cascade chemotherapy. Furthermore, H&E (hematoxylin and eosin) staining of tumor slices (Figure 5g) confirmed prominently enhanced necrosis in the group of A@UiO-66-H-P plus laser exposure compared with the other groups. These results collectively demonstrated that such combined therapy triggered by O_2-depleting PDT is a potent strategy to eradicate tumor. In this nanosystem, the localized therapeutic effect of PDT, limited premature release of prodrug, and stimuli-triggered chemotherapy were also beneficial to alleviate side effects. This was supported by monitoring the body weight and evaluating the damage of the NPs to normal tissues. No significant decrease in body weight of mice was observed during the treatments (Figure S27, Supporting Information). Meanwhile, H&E staining analysis of the major organs slices showed little to no pathological abnormity in each treatment (Figure S28, Supporting Information), which further proved the biocompatibility of the NPs, highlighting their potential application for cancer treatments with negligible systemic toxicity.

3. Conclusions

In summary, we fabricated multifunctional UiO-66-H-P NMOFs for efficient prodrug loading and demonstrated them to be potent nanocarriers to preserve the stability of prodrug. In vitro prodrug release profile indicated the on-demand AQ4N release

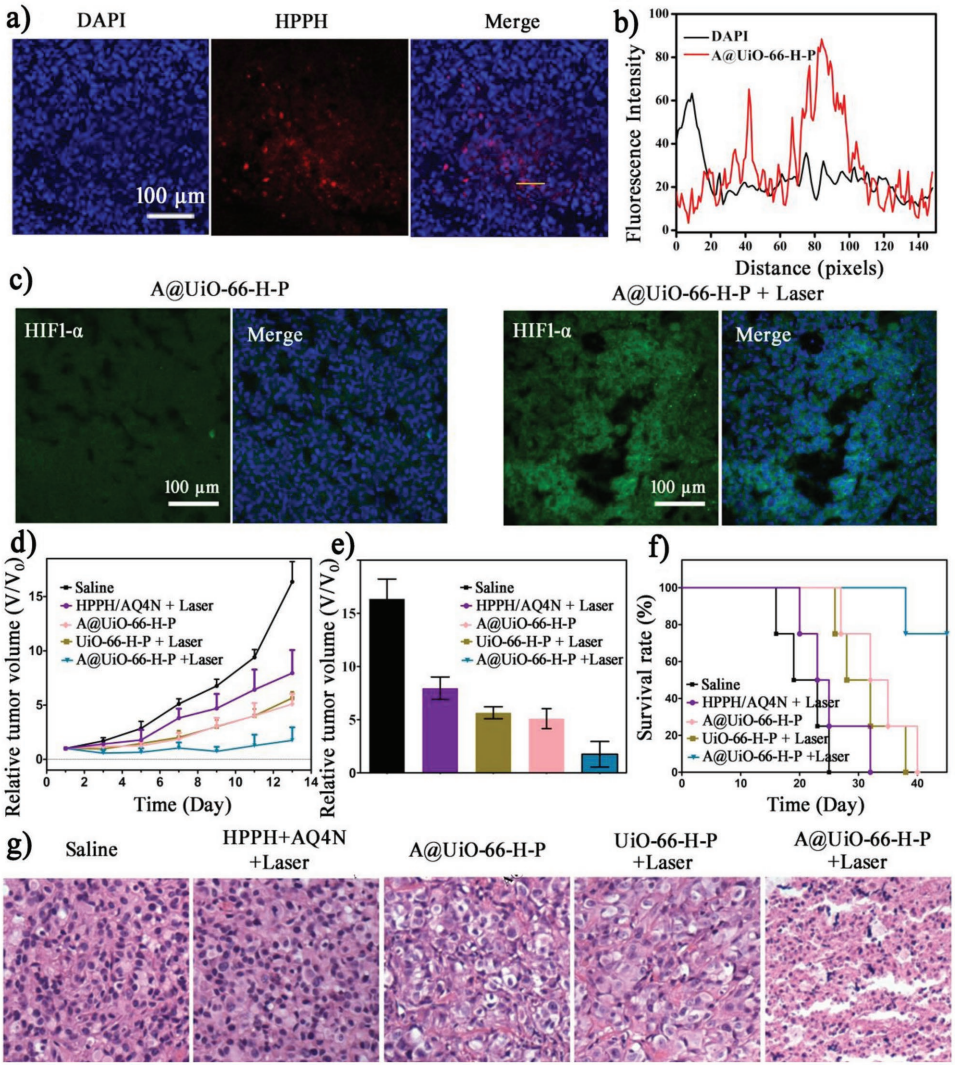

Figure 5. a) CLSM images of the tumor slice collected at 24 h after i.v. injection of A@UiO-66-H-P. Blue, DAPI-stained nucleus; Red, HPPH of A@UiO-66-H-P. b) Fluorescence intensity of A@UiO-66-H-P along the marked line in the left merged image. c) HIF1-α immunofluorescence staining of the tumor slices collected from A@UiO-66-H-P treated mice with or without laser exposure. d) Tumor volume growth curves during treatments ($n = 5$). e) The relative tumor volume from the mice received different treatments on day 13 after treatment. f) Survival rate of U87MG tumor-bearing mice after different treatments. g) H&E observation of tumor section collected on day 13 from the mice treated with different formulations.

behavior of the NPs. Additionally, in vivo studies revealed that the i.v. injection of A@UiO-66-H-P followed by laser exposure indeed intensified tumor hypoxia which favored the activation of chemotherapy. Such PDT-induced and hypoxia-activated process improves the therapeutic efficacy, holding great promise for effective cancer treatment.

4. Experimental Section

Materials: Zirconium(IV) chloride ($ZrCl_4$), terephthalic acid, benzoic acid, 4-(bromomethyl)benzoic acid, sodium azide, DCFH-DA, and AQ4N were purchased from Sigma-Aldrich. HPPH was bought from Medkoo Bioscience, Inc. PEG-NH_2 was obtained from Biochempeg Scientific Inc. Live/dead viability kit was supplied by Thermo Fisher Scientific. HIF1-α monoclonal antibody and goat anti-rat IgG (H+L) secondary antibody with Alexa Fluor 488 modification were bought from Invitrogen. All the above chemicals were used without further purification. Ultrapure water was prepared using a Milli-Q purification system from Millipore.

Characterization: TEM images were obtained from a Tecnai TF30 transmission electron microscope (FEI, Hillsboro, OR). Scanning electron microscope (SEM) images were acquired from a Hitachi SU-70 Schottky field emission gun scanning electron microscope (FEG-SEM). UV–vis spectra were recorded on a Genesys 10s UV–vis spectrophotometer (Thermo Scientific, Waltham, MA). ^{1}H-NMR measurement was operated on a Bruker AV300 scanner using $CDCl_3$ as the solvent. The chemical shifts (δ) were expressed in parts per million (ppm). FTIR spectra were acquired from a Nicolet 6700 FT-IR spectrometer (Thermo Scientific, USA). The diameter distribution was measured via a scientific nanoparticle analyzer (SZ-100, Horiba). PXRD data were obtained from a D8 ADVANCE X-Ray Powder Diffractometer (Bruker, German). Nitrogen adsorption–desorption isotherm was carried out on a Micromeritics ASAP 2020M automated sorption analyzer (Micromeritics Co., USA). Prior to measurement, the samples were degassed at 120 °C for 24 h. The specific surface areas were

determined based on the N_2 adsorption isotherm at 77 K by Brunauer–Emmett–Teller (BET) method. And the corresponding size distribution was obtained using the density functional theory (DFT) model. The HPLC analysis was performed on a Agilent1200 machine (Agilent, USA). The quantification of zirconium was conducted using ICP-OES (Agilent 720-ES). CLSM images were recorded on a Zeiss LSM 780 microscope. Flow cytometry analysis was performed on BD Beckman Coulter flow cytometer (Brea, CA).

Synthesis of p-Azidomethylbenzoic Acid: 4-(Bromomethyl)benzoic acid (5.00 g) and NaN_3 (7.00 g) were added into DMF (50 mL), and the mixture was stirred at 65 °C for 24 h. After cooling down, 100 mL ultrapure water was poured into the above solvent, which led to the precipitation of white product. The precipitate was collected by filtration, washed with cold water (3 × 30 mL), and dried under vacuum to give *p*-azidomethylbenzoic acid as a white solid, which was stored in −20 °C for further use.

Synthesis of DBCO-PEG: NH_2-PEG (500 mg) and DBCO-NHS (60.0 mg) were dissolved in 4 mL of chloroform. Then 30 µL of trimethylamine was added immediately and the mixture was stirred overnight. After that, the product was precipitated from diethyl ether. White powder was gained after centrifugation and further washed with diethyl ether (3 × 30 mL).

Preparation of A@UiO-66-H-P: The fabrication process was divided into three steps: (1) one-pot synthesis of UiO-66-H/N_3, (2) AQ4N encapsulation, and (3) PEGylation. Briefly, UiO-66-H/N_3 was prepared as follows: $ZrCl_4$ (10.5 mg), terephthalic acid (5.48 mg), *p*-azidomethylbenzoic acid (23.4 mg), and HPPH (21.0 mg) were dissolved into DMF (2 mL) in a Pyrex vial. Then the mixture was added with 60 µL of acetic acid and subsequently heated at 90 °C for 24 h. Afterward, the resultant NPs were collected by centrifugation and washed with DMF for several times. To extract the residual DMF within the pores of the NPs, the precipitate was immersed in acetone for 24 h. This removal process was repeated twice. For AQ4N loading, 1.00 mg of UiO-66-H/N_3 NPs was dispersed into 1 mL AQ4N-containing aqueous solution (350 µg mL^{-1}). After stirring for 1 d, the aqueous solution was added with DBCO-PEG (10.0 mg), and the mixture was stirred for additional 6 h. Unbound AQ4N and unreacted DBCO-PEG were removed after centrifugation. The unloaded AQ4N in the supernatant was quantified using UV–vis measurement, according to which the AQ4N loading capacity was determined.

Stability Test of the UiO-66-N_3 NPs: 200 µL of UiO-66-N_3 (5.00 mg mL^{-1}) was added into a dialysis tube (10 000 MWCO) (Slide-A-Lyzer, Thermo Scientific) against 1.3 mL of 2.00×10^{-3} M PBS (pH 7.4). At predetermined time intervals, the whole buffer solution was collected for HPLC measurement, followed by supplying with 1.3 mL of fresh PBS buffer. The amount of the released *p*-azidomethylbenzoic acid was quantified by HPLC with a C18 column (5 µm, 4.6 × 150 mm) at a flow rate of 1 mL min^{-1}. 60% mobile phase A (ultrapure water plus 0.1% trifluoroacetic acid) and 40% mobile phase B (0.1% trifluoroacetic acid-containing acetonitrile) were used in these experiments. The elution was monitored according to the absorption at 228 nm. To determine the total content of *p*-azidomethylbenzoic acid on the UiO-66-N_3 NPs, the NPs (1.00 mg) were decomposed by aqua regia and the released *p*-azidomethylbenzoic acid was taken as the whole amount.

In Vitro Prodrug Release: The phosphate ions-sensitive AQ4N release was studied by comparing the AQ4N release in different concentrations of PBS buffers (pH 7.4). Typically, 2.00 mg of A@UiO-66-H-P NPs were dispersed in PBS buffers (2.00, 10.0, or 50.0×10^{-3} M), respectively. At predetermined time intervals, 100 µL of the solution was withdrawn and subjected to centrifugation (15 000 rpm, 15 min). Then 60 µL of the supernatant as the liberated AQ4N was collected, and quantified by a plate reader based on the absorption at 594 nm. According to a standard curve, the release percentage of AQ4N was calculated.

Cell Culture and Animal Model: Human glioblastoma cell line U87MG was purchased from American Type Culture Collection (ATCC) and maintained in minimum Eagle's medium (MEM) medium supplemented with FBS (10%) and streptomycin (100 µg mL^{-1}) and penicillin (100 µg mL^{-1}). The cells were placed in a 37 °C humidified incubator with 5% CO_2 supply. To build U87MG tumor model, U87MG cells (4×10^6) were subcutaneously injected into the flank of female nude mice. The tumor-bearing mice were used for antitumor studies until the tumor volumes reached about 100 mm^3. All the animal use abided by the protocol permitted by the National Institutes of Health Clinical Center Animal Care and Use Committee.

Confocal Fluorescence Imaging: For confocal imaging, cells were plated on a confocal dishes for 24 h, and subjected to various treatments. After that, U87MG cells were rinsed with sterile PBS and prepared for imaging. Typically, to study the cellular uptake, the cells were fixed with Z-fix solution after treatments with A@UiO-66-H-P and subsequently mounted with DAPI-containing mounting medium. To study the endocytic pathway, the cells in the inhibition groups were preincubated with serum-free MEM medium containing sucrose (225×10^{-3} M), amiloride (1.00×10^{-3} M), or genistein (25.0 µg mL^{-1}). 30 min later, the medium was replaced with fresh medium containing the corresponding inhibitor plus A@UiO-66-H-P and further incubated for 1 h in the 37 °C incubator with 5% CO_2/95% air supply. Afterward, the cells were fixed with Z-fix solution and observed by CLSM. For endosome/lysosomes localization of A@UiO-66-H-P, the cells were cultured with the NPs for 3 h, and further incubated with LysoTracker Green (1.5×10^{-6} M) for 30 min. After washing with PBS for three times, the cells were subjected to CLSM observation. The intracellular ROS was measured followed a reported strategy.[7] As for intracellular O_2 detection, U87MG cells were preincubated with $[Ru(dpp)_3]Cl_2$ (5.00×10^{-6} M) for 4 h, followed by treatments with different samples for 15 h. After laser exposure, the cells were rinsed several times with PBS and fixed using Z-fix solution for confocal fluorescence imaging. The excitation wavelength was set as 488 nm, and the fluorescence emission ranging from 600 to 650 nm was collected by confocal microscopy.

Flow Cytometry Analysis: Cellular uptake and intracellular ROS level were explored by flow cytometry assay. After different treatments, cells were harvested, rinsed, and suspended in PBS for flow cytometry analysis. Each experiment counted more than 10 000 cells, and the data were analyzed by means of FlowJo Software.

In Vitro Cytotoxicity Study: MTT assay was employed to confirm the hypoxia-activated toxicity of AQ4N as well as the combination therapy of UiO-66-H/N_3 NPs. To test the hypoxia-induced toxicity of AQ4N, U87MG cells with a density of 2000 per well were seeded in 96-well plates for 24 h, and subsequently incubated with AQ4N or A@UiO-66-H-P NPs at various concentrations. The plates were placed in hypoxic or normoxic incubator for 24 h. Afterward, all the cells were cultured in normoxic incubator for another 48 h. Finally, 10 µL of MTT (5.00 mg mL^{-1}) was added to each well and further cultured for 4 h. The medium was then replaced with 100 µL of DMSO to dissolve formazan crystals. The cell survival rate was calculated using the absorption at 490 nm measured by a plate reader. In order to evaluate the therapeutic effect, U87MG cells were seeded in 96-well plates at 40 000 mL^{-1} (100 µL). After 24 h incubation, the cells were treated with free AQ4N, UiO-66-H-P, or A@UiO-66-H-P NPs for 24 h followed by laser irradiation at 671 nm (100 mW cm^{-2}, 6 min). The plates were placed in incubator for additional 36 h. Analogously, the cell viability was determined using MTT assay.

Live/Dead Cell Viability Assay: U87MG cells with a density of 40 000 mL^{-1} (200 µL) were plated onto eight-well chamber slides for 24 h. Then the cells were treated with UiO-66-H-P or A@UiO-66-H-P NPs and selectively exposed to laser irradiation (100 mW cm^{-2}, 6 min). Then, the chambers were put into an incubator for additional 36 h. The medium was substituted with the mixed solution of calcium AM (2.00×10^{-6} M) and PI (4.00×10^{-6} M). After 30 min incubation, the slices were rinsed, prepared, and imaged by a fluorescence microscope.

Multicellular Tumor Spheroids Model: 96-well spheroid plates (Corning) were employed to set up multicellular tumor spheroids model. Typically, U87MG cells were cultured for several days. When the diameter of the spheroids reached ≈400 µm, the medium was replaced with A@UiO-66-H-P NPs (50.0 µg mL^{-1}) in fresh medium for another 24 h. After careful washing, the spheroids were fixed, immersed with DAPI-containing mounting medium, and visualized by confocal imaging.

HIF1-α Immunofluorescence Analysis: HIF-1α staining was carried out to verify PDT-induced sever hypoxia at tumor site. Briefly, U87MG

tumor-bearing mice were intravenously injected with A@UiO-66-H-P NPs and selectively received 671 nm laser irradiation (100 mW cm^{-2}) for 6 min at 24 h postinjection. Afterward, the mice with or without laser exposure were sacrificed to collect tumor sections which were fixed with paraformaldehyde for 15 min, permeabilized using 0.1% triton X-100 in 0.1% sodium citrate for 15 min, and blocked with 2% BSA in PBS buffer for 30 min. The tumor slices were then incubated with HIF1-α monoclonal antibody according to the manufacturer's instructions. After rinsing with PBS, the sections were stained with Alexa Fluor 488-modified goat anti-rat IgG (H+L) secondary antibody and further mounted with DAPI-containing mounting medium. Finally, the slices were prepared for confocal observation.

In Vivo Therapeutic Effects: When tumor size reached ≈100 mm^3, U87MG tumor-bearing mice were randomly divided into five groups and administrated with various formulations: (1) saline; (2) the mixture of HPPH and AQ4N followed by laser irradiation; (3) UiO-66-H-P followed by laser exposure; (4) A@UiO-66-H-P; (5) A@UiO-66-H-P followed by laser irradiation. In these experiments, all the samples were prepared using saline solution, and the laser (671 nm, 100 mW cm^{-2}, 10 min) was selectively applied at tumor sites at 24 h postinjection. During the treatments, the mice were weighted every other days. The tumor size was measured and computed following the formula: $V = LW^2/2$, where L and W represent the length and width of tumor, respectively.

Supporting Information

Supporting Information is available from the Wiley Online Library or from the author.

Acknowledgements

Z.H. and Y.D. contributed equally to this work. This research was funded by the National Natural Science Foundation of China (21335004, 21605118) and Intramural Research Program of the National Institute of Biomedical Imaging and Bioengineering, National Institutes of Health. Z.H. (201606190118) also appreciates the support from China Scholarship Council (CSC).

Conflict of Interest

The authors declare no conflict of interest.

Keywords

banoxantrone, cascade therapy, hypoxia-activated prodrugs, nanoscale metal–organic frameworks, photodynamic therapy

Received: October 7, 2018
Revised: November 9, 2018
Published online: December 19, 2018

[1] X. H. Yu, D. Gao, L. Q. Gao, J. H. Lai, C. R. Zhang, Y. Zhao, L. J. Zhong, B. Jia, F. Wang, X. Y. Chen, Z. F. Liu, *ACS Nano* **2017**, *11*, 10147.
[2] K. R. Deng, C. X. Li, S. S. Huang, B. G. Xing, D. Y. Jin, Q. G. Zeng, Z. Y. Hou, J. Lin, *Small* **2017**, *13*, 1702299.
[3] J. Park, Q. Jiang, D. W. Feng, L. Q. Mao, H.-C. Zhou, *J. Am. Chem. Soc.* **2016**, *138*, 3518.
[4] A. P. Thomas, L. Palanikumar, M. T. Jeena, K. Kim, J.-H. Ryu, *Chem. Sci.* **2017**, *8*, 8351.
[5] Z. H. Xiang, L. Zhu, L. Qi, L. Yan, Y. H. Xue, D. Wang, J.-F. Chen, L. M. Dai, *Chem. Mater.* **2016**, *28*, 8651.
[6] Y. H. Cheng, H. Cheng, C. X. Jiang, X. F. Qiu, K. K. Wang, W. Huan, A. H. Yuan, J. H. Wu, Y. Q. Hu, *Nat. Commun.* **2015**, *6*, 8785.
[7] Z. M. He, Y. Xiao, J.-R. Zhang, P. H. Zhang, J.-J. Zhu, *Chem. Commun.* **2018**.
[8] X. J. Song, L. Z. Feng, C. Liang, M. Gao, G. S. Song, Z. Liu, *Nano Res.* **2017**, *10*, 1200.
[9] Z. L. Dong, L. Z. Feng, Y. Hao, M. C. Chen, M. Gao, Y. Chao, H. Zhao, W. W. Zhu, J. J. Liu, C. Liang, Q. Zhang, Z. Liu, *J. Am. Chem. Soc.* **2018**, *140*, 2165.
[10] W.-X. Qiu, L.-H. Liu, S.-Y. Li, Q. Lei, G.-F. Luo, X.-Z. Zhang, *Small* **2017**, *13*, 1603956.
[11] T. Guo, Y. Wu, Y. Lin, X. Xu, H. Lian, G. M. Huang, J.-Z. Liu, X. P. Wu, H.-H. Yang, *Small* **2018**, *14*, 1702815.
[12] H. R. Wang, Y. Chao, J. J. Liu, W. W. Zhu, G. L. Wang, L. G. Xu, Z. Liu, *Biomaterials* **2018**, *181*, 310.
[13] D. L. Tao, L. Z. Feng, Y. Chao, C. Liang, X. J. Song, H. R. Wang, K. Yang, Z. Liu, *Adv. Funct. Mater.* **2018**, *28*, 1804901.
[14] J. Lin, S. J. Wang, P. Huang, Z. Wang, S. H. Chen, G. Niu, W. W. Li, J. He, D. X. Cui, G. M. Lu, X. Y. Chen, Z. H. Nie, *ACS Nano* **2013**, *7*, 5320.
[15] M. Chen, X. L. Liang, C. Gao, R. R. Zhao, N. S. Zhang, S. M. Wang, W. Chen, B. Zhao, J. R. Wang, Z. F. Dai, *ACS Nano* **2018**.
[16] P. Prasad, C. R. Gordijo, A. Z. Abbasi, A. Maeda, A. Ip, A. M. Rauth, R. S. DaCosta, X. Y. Wu, *ACS Nano* **2014**, *8*, 3202.
[17] H. C. Chen, J. W. Tian, W. J. He, Z. J. Guo, *J. Am. Chem. Soc.* **2015**, *137*, 1539.
[18] M. L. Song, T. Liu, C. R. Shi, X. Z. Zhang, X. Y. Chen, *ACS Nano* **2016**, *10*, 633.
[19] C. R. Gordijo, A. Z. Abbasi, M. A. Amini, H. Y. Lip, A. Maeda, P. Cai, P. J. O'Brien, R. S. DaCosta, A. M. Rauth, X. Y. Wu, *Adv. Funct. Mater.* **2015**, *25*, 1858.
[20] S.-Y. Li, H. Cheng, B.-R. Xie, W.-X. Qiu, J.-Y. Zeng, C.-X. Li, S.-S. Wan, L. Zhang, W.-L. Liu, X.-Z. Zhang, *ACS Nano* **2017**, *11*, 7006.
[21] L. Z. Feng, L. Cheng, Z. L. Dong, D. L. Tao, T. E. Barnhart, W. B. Cai, M. W. Chen, Z. Liu, *ACS Nano* **2017**, *11*, 927.
[22] D. Zhang, A. X. Zheng, J. Li, M. Wu, L. J. Wu, Z. W. Wei, N. S. Liao, X. L. Zhang, Z. X. Cai, H. H. Yang, G. Liu, X. L. Liu, J. F. Liu, *Theranostics* **2017**, *7*, 164.
[23] Y. Z. Wang, Y. Xie, J. Li, Z.-H. Peng, Y. Sheinin, J. P. Zhou, D. Oupický, *ACS Nano* **2017**.
[24] Y. Y. Liu, Y. Liu, W. B. Bu, C. Cheng, C. J. Zuo, Q. F. Xiao, Y. Sun, D. L. Ni, C. Zhang, J. N. Liu, J. L. Shi, *Angew. Chem., Int. Ed.* **2015**, *54*, 8105.
[25] R. M. Phillips, *Cancer Chemother. Pharmacol.* **2016**, *77*, 441.
[26] C. R. Nishida, P. R. Ortiz de Montellano, *J. Med. Chem.* **2008**, *51*, 5118.
[27] S. M. Raleigh, E. Wanogho, M. D. Burke, S. R. McKeown, L. H. Patterson, *Int. J. Radiat. Oncol., Biol., Phys.* **1998**, *42*, 763.
[28] J. Della Rocca, D. M. Liu, W. B. Lin, *Acc. Chem. Res.* **2011**, *44*, 957.
[29] C. B. He, D. M. Liu, W. B. Lin, *Chem. Rev.* **2015**, *115*, 11079.
[30] L. Valenzano, B. Civalleri, S. Chavan, S. Bordiga, M. H. Nilsen, S. Jakobsen, K. P. Lillerud, C. Lamberti, *Chem. Mater.* **2011**, *23*, 1700.
[31] S. Chavan, J. G. Vitillo, D. Gianolio, O. Zavorotynska, B. Civalleri, S. Jakobsen, M. H. Nilsen, L. Valenzano, C. Lamberti, K. P. Lillerud, S. Bordiga, *Phys. Chem. Chem. Phys.* **2012**, *14*, 1614.
[32] C. B. He, K. D. Lu, D. M. Liu, W. B. Lin, *J. Am. Chem. Soc.* **2014**, *136*, 5181.
[33] I. A. Lazaro, S. Haddad, S. Sacca, C. Orellana-Tavra, D. Fairen-Jimenez, R. S. Forgan, *Chem* **2017**, *2*, 561.

[34] M.-X. Wu, J. Gao, F. Wang, J. Yang, N. Song, X. Y. Jin, P. Mi, J. Tian, J. Y. Luo, F. Liang, Y.-W. Yang, *Small* **2018**, *14*, 1704440.
[35] M.-X. Wu, H.-J. Yan, J. Gao, Y. Cheng, J. Yang, J.-R. Wu, B.-J. Gong, H.-Y. Zhang, Y.-W. Yang, *ACS Appl. Mater. Interfaces* **2018**, *10*, 34655.
[36] A. Umemura, S. Diring, S. Furukawa, H. Uehara, T. Tsuruoka, S. Kitagawa, *J. Am. Chem. Soc.* **2011**, *133*, 15506.
[37] F. Vermoortele, B. Bueken, G. Le Bars, B. Van de Voorde, M. Vandichel, K. Houthoofd, A. Vimont, M. Daturi, M. Waroquier, V. Van Speybroeck, C. Kirschhock, D. E. De Vos, *J. Am. Chem. Soc.* **2013**, *135*, 11465.
[38] H. L. Guo, Y. Z. Zhu, S. Wang, S. Q. Su, L. Zhou, H. J. Zhang, *Chem. Mater.* **2012**, *24*, 444.
[39] J. Park, Q. Jiang, D. W. Feng, H.-C. Zhou, *Angew. Chem., Int. Ed.* **2016**, *55*, 7188.
[40] L. L. Hill, *Pediatr. Clin. North Am.* **1990**, *37*, 241.
[41] J. Park, Z. U. Wang, L.-B. Sun, Y.-P. Chen, H.-C. Zhou, *J. Am. Chem. Soc.* **2012**, *134*, 20110.
[42] H. K. Yoon, X. Lou, Y.-C. Chen, Y.-E. K. Lee, E. Yoon, R. Kopelman, *Chem. Mater.* **2014**, *26*, 1592.
[43] J. T. Dy, K. Ogawa, A. Satake, A. Ishizumi, Y. Kobuke, *Chem. - Eur. J.* **2007**, *13*, 3491.
[44] J. Wang, G. Z. Zhu, M. X. You, E. Q. Song, M. I. Shukoor, K. J. Zhang, M. B. Altman, Y. Chen, Z. Zhu, C. Z. Huang, W. H. Tan, *ACS Nano* **2012**, *6*, 5070.
[45] A. Apirakaramwong, P. Pamonsinlapatham, S. Techaarpornkul, P. Opanasopit, S. Panomsuk, S. Soksawatmaekhin, *Adv. Mater. Res.* **2012**, *506*, 485.
[46] G. C. Yu, M. M. Zhang, M. L. Saha, Z. W. Mao, J. Chen, Y. Yao, Z. J. Zhou, Y. J. Liu, C. Y. Gao, F. H. Huang, X. Y. Chen, P. J. Stang, *J. Am. Chem. Soc.* **2017**, *139*, 15940.
[47] C. Orellana-Tavra, S. A. Mercado, D. Fairen-Jimenez, *Adv. Healthcare Mater.* **2016**, *5*, 2261.
[48] R. Röder, T. Preiß, P. Hirschle, B. Steinborn, A. Zimpel, M. Höhn, J. O. Rädler, T. Bein, E. Wagner, S. Wuttke, U. Lächelt, *J. Am. Chem. Soc.* **2017**, *139*, 2359.
[49] Y. Zhang, F. M. Wang, C. Q. Liu, Z. Z. Wang, L. H. Kang, Y. Y. Huang, K. Dong, J. S. Ren, X. G. Qu, *ACS Nano* **2018**, *12*, 651.
[50] D.-W. Zheng, B. Li, C.-X. Li, J.-X. Fan, Q. Lei, C. Li, Z. S. Xu, X.-Z. Zhang, *ACS Nano* **2016**, *10*, 8715.
[51] Z. F. Ma, X. D. Jia, J. Bai, Y. D. Ruan, C. Wang, J. M. Li, M. C. Zhang, X. E. Jiang, *Adv. Funct. Mater.* **2017**, *27*, 1604258.
[52] X. L. Cun, M. Li, S. Y. Wang, Y. F. Wang, J. L. Wang, Z. Z. Lu, R. X. Yang, X. Tang, Z. R. Zhang, Q. He, *Nanoscale* **2018**, *10*, 9935.
[53] H.-J. Li, J.-Z. Du, X.-J. Du, C.-F. Xu, C.-Y. Sun, H.-X. Wang, Z.-T. Cao, X.-Z. Yang, Y.-H. Zhu, S. M. Nie, J. Wang, *Proc. Natl. Acad. Sci. USA* **2016**, *113*, 4164.
[54] W. Tang, Z. Yang, S. Wang, Z. T. Wang, J. B. Song, G. C. Yu, W. P. Fan, Y. L. Dai, J. J. Wang, L. L. Shan, G. Niu, Q. L. Fan, X. Y. Chen, *ACS Nano* **2018**, *12*, 2610.